chemosensors

MDPI

Article

SERS of Human Red Blood Cells in Non-Resonant Conditions: Benefits, Limitations, and Complementary Tools (CytoViva and GFAAS)

Kelsey L. Wells [1], Praveen K. Alla [1], Kyra G. Kaiser [2], Ioana T. Murgulet [2], Norma C. Adragna [1] and Ioana E. Pavel [2,*]

[1] Department of Chemistry and Department of Pharmacology and Toxicology, Wright State University, 3640 Colonel Glenn Hwy., Dayton, OH 45435-0001, USA; kelsey.wells@wcs.edu (K.L.W.)
[2] Department of Physical and Environmental Sciences, Texas A&M University Corpus Christi, 6300 Ocean Drive, Corpus Christi, TX 78412-5800, USA
* Correspondence: ioana.pavel@tamucc.edu; Tel.: +1-361-825-3824

Abstract: Herein, Raman and surface-enhanced Raman spectroscopies (SERS) were successfully employed to establish the chemical interactions of citrate-capped silver nanoparticles (AgNPs, 10–15 nm) with human red blood cells (RBCs). The Raman/SERS spectra offered spectral evidence for the cellular uptake of AgNPs and the subsequent change in the conformation of the most abundant component, hemoglobin (Hb), from oxyhemoglobin to deoxyhemoglobin. The spectral characterization of AgNPs' interactions with other RBC biomarkers (membrane proteins and lipids) was impeded by the dominant Hb bands, even for non-resonant Hb conditions. CytoViva hyperspectral imaging and graphite furnace atomic absorption spectroscopy (GFAAS) served as complementary tools to effectively address the challenges related to a single excitation line (632.8 nm) and the resolution of the confocal Raman microscope (0.5–1.0 μm). CytoViva confirmed the RBC-AgNP interactions through hyperspectral signatures and facilitated the label-free localization of AgNPs extracellularly and intracellularly. Irreversible agglutination of RBCs was noted after 24 h of exposure, raising concerns about the toxicity of AgNPs of biocompatible citrate coatings. GFAAS validated the Raman/SERS results by quantifying the proportion of AgNPs absorbed by RBCs, which was significant (~48% AgNPs by mass), mostly at the membrane (60% RBCs), and size dependent (no large AgNPs or AgNP-aggregates in RBCs, after 12–24 h).

Keywords: red blood cells; silver nanoparticles; surface enhanced Raman spectroscopy (SERS); CytoViva hyperspectral imaging; graphite furnace atomic absorption spectroscopy (GFAAS)

Citation: Wells, K.L.; Alla, P.K.; Kaiser, K.G.; Murgulet, I.T.; Adragna, N.C.; Pavel, I.E. SERS of Human Red Blood Cells in Non-Resonant Conditions: Benefits, Limitations, and Complementary Tools (CytoViva and GFAAS). *Chemosensors* **2023**, *11*, 353. https://doi.org/10.3390/chemosensors11070353

Academic Editors: Cristina M. Muntean and Sanda Boca-Farcău

Received: 6 May 2023
Revised: 17 June 2023
Accepted: 19 June 2023
Published: 21 June 2023

1. Introduction

Raman spectroscopy [1] has attracted great attention due to its nondestructive, molecular fingerprinting capabilities under biocompatible conditions. In Raman spectroscopy, structurally similar molecules that have the same fluorescence emission profiles can yield distinct Raman spectra with narrow peaks, enabling multiplex detection with a single excitation line [1,2]. Furthermore, surface-enhanced Raman spectroscopy (SERS) [2–7], an embodiment of Raman spectroscopy, can lower the detection limits of Raman down to the single-molecule level. The Raman cross-sections (10^{-30}–10^{-25} cm^2 per molecule) may be increased by as much as 14 orders of magnitude in SERS, when targeted molecules reside near or at the interstitial sites of nanostructured systems composed of certain metals, such as silver or gold nanoparticles (AgNPs or AuNPs) [1,3,4]. The favorable locations for exciting intense SERS are often referred to as SERS "hot spots"; they largely arise from the increase in the magnitude of both the incident and scattered electromagnetic fields associated with the excitation of coupled, localized surface plasmon resonances (LSPR) of aggregated AgNPs [1,3,4].

Confocal Raman spectroscopy and SERS have been demonstrated to be powerful bioanalytical techniques for the characterization and detection of blood and its key components, such as red blood cells (RBCs) [8–19]. For example, resonance Raman spectroscopy helped elucidate the high symmetry and chromophoric structure of hemoglobin (Hb) and its derivatives in RBCs when excited with laser wavelengths resonant or nearly resonant with the electronic transitions of the heme group (e.g., the Soret electronic transition at 417 nm) [10]. Other biomarkers of RBCs, such as membrane proteins and lipids, can become detectable under non-resonant Hb conditions, while shifting the excitation line from the near-ultraviolet range (417 nm) toward the near-infrared range (1064 nm). However, the simultaneous characterization of these main RBC components (cytoplasmic Hb versus membrane biomarkers) can be challenging due to the dominant nature of the Hb modes (Hb is the most abundant RBC component by dry weight). Thus, Hb bands tend to mask most spectral contributions of the membrane proteins and lipids even for non-resonant conditions (e.g., the 1640 cm^{-1} marker band of both the amide I of proteins and the $C_\alpha C_m$ groups of Hb in the spin-state spectral region) [10].

In this study, we propose to overcome these limitations of Raman spectroscopy associated with the usage of a single, non-resonant Hb excitation line and a typical confocal Raman microscope. To achieve this, Raman and SERS analyses of controls and samples of human RBCs exposed to AgNPs under non-resonant Hb conditions will be complemented by CytoViva hyperspectral imaging and graphite furnace atomic absorption spectroscopy (GFAAS) measurements. A laser wavelength of 632.8 nm (HeNe) was selected for the excitation of RBCs under non-resonant Hb conditions. Most Raman systems designed for biomedical and material characterization applications are equipped with similar red or near-infrared lasers due to reduced photodamage, affordable cost, and suppression of unwanted fluorescence emissions (e.g., autofluorescence of RBCs across multiple wavelengths). The sensitivity of the Raman method will be amplified by harvesting the SERS effects of AgNPs. Thus, citrate-capped AgNPs will be synthesized, size-selected, purified, and concentrated by tangential flow filtration (TFF) for improved homogeneity in the SERS experiments with RBCs. These small AgNPs with an average diameter of 10–15 nm were selected as a nano-model due to their recognized biocompatible coating and capability of penetrating RBC membranes [12,18]. Furthermore, the citrate capping agent is also a major component of the common anticoagulant CPD solution (citrate, phosphate, and dextrose) used to temporarily store the human RBCs of this study. SERS of human blood has been successfully employed in clinical diagnostics (e.g., detection of malaria and oral squamous cell carcinoma) [8,19], and forensics (e.g., blood identification by swabbing the SERS substrate directly onto the mock evidence) [9]. Herein, it is expected that SERS under non-resonant Hb conditions will confirm the internalization of AgNPs and provide detailed information about the chemical interactions of AgNPs with both cytoplasmic (Hb) and membrane RBC components (e.g., proteins and lipids). Furthermore, GFAAS will validate the Raman and SERS data by quantifying the total cellular uptake of AgNPs (extracellularly and intracellularly). Additionally, CytoViva hyperspectral imaging will offer direct, label-free visual and indirect hyperspectral confirmations of AgNPs' localization within the cellular matrix. CytoViva enhanced darkfield microscope optics are designed to enable the observation of nanomaterials as small as 10–20 nm in diameter, in biological environments, and thereby, to surpass the spatial resolution of confocal Raman microscopes (i.e., 0.5–1.0 μm in this study).

2. Materials and Methods

2.1. Chemicals

Most reagents, including silver nitrate ($AgNO_3$), trisodium citrate ($Na_3C_6H_5O_7$ $2H_2O$), rhodamine 6G (R6G), D-glucose, hydrogen peroxide (30% H_2O_2), Hematoseal, ICP-OES grade Ag^+ standard (SPEX CertPrep, 1000 ± 5 mg L^{-1}), and OPTIMA grade nitric acid (HNO_3), for trace metal analysis were purchased from Fisher Scientific (part of Thermo Fisher Scientific, Waltham, MA, USA). Phosphate-buffered saline (PBS, 10×, pH of 7.4 ± 0.1)

was obtained from Fisher Bioreagents (part of Thermo Fisher Scientific, Waltham, MA, USA). High-quality water (18 MΩ cm) was used throughout all experiments.

2.2. Synthesis of Silver Nanoparticles (AgNPs)

Citrate-capped AgNPs were prepared using a modified Lee–Meisel synthesis technique to obtain small, quasi-spherical AgNPs [20,21]. Briefly, 1.7 mL of a 1% silver nitrate solution was added to 100 mL of water and the solution was heated at ~90 °C with continuous stirring, for about 15 min. Then, ~2 mL of a 1% trisodium citrate solution was slowly pipetted in and heating was continued for 1 h with stirring. The resulting colloid was stored at 10 °C and used when fresh.

2.3. Tangential Flow Filtration (TFF) of AgNPs

A 1 L-batch of colloidal AgNPs was processed using a tangential flow filtration system (Repligen Inc., Waltham, MA, USA) and two modified polyether sulfone (mPES) filters, as previously described in our work [22,23]. First, the original colloid was run through a 500 kD filter (MidiKros, 790 cm^2). The resulting 100 kD permeate containing AgNPs smaller than ~50 nm in diameter was then processed through a 10 kD filter (MiniKros, 790 cm^2). The final 10 kD retentate containing AgNPs with diameters larger than 5 nm and smaller than 50 nm was then characterized for further use in the SERS experiments with RBCs.

2.4. Exposure of Human Red Blood Cells (RBCs) to AgNPs, Cell Counting, and Hematocrit

Packed human RBCs were obtained from the Community Blood Center of Dayton, Ohio (Dayton, OH, USA). The blood (type AB^+) was donated by healthy volunteers. The blood was prescreened for numerous pathogens including hepatitis B virus (HBV), hepatitis C virus (HCV), human immunodeficiency virus types 1 and 2 (HIV-1 and HIV-2), *Treponema pallidum* (syphilis), human T-cell lymphotropic virus types I and II (HTLV), West Nile virus (WNV), *Trypanosoma cruzi* (Chagas disease), and Zika virus. RBCs were collected in vacutainer tubes (K_2EDTA) and were stored at 4 °C. Prior to use, the anticoagulant (CPD) and preservation solutions (mostly Optisol, AS-5) were separated from RBCs by centrifugation (10,000 rpm or $7.8 \times 10^3 \times g$) in 1 mL of 1× PBS for 10 min. The washing process was repeated thrice, while the PBS was kept at 4 °C. Washed RBCs were dispersed into a suspension of filtered AgNPs in 5% glucose and incubated at 37 °C, for one hour, with gentle agitation every 15 min, or at 4 °C, up to 24 h. The RBCs-to-5% glucose ratio was optimized to resemble that of plasma in the human body by maintaining an osmolality of ~290 mOSM (isosmotic). The final concentration of AgNPs was 15 μg mL^{-1}. Afterward, RBCs were separated and washed thrice with 5% glucose via centrifugation at 3000 rpm, for 10 min each time. The controls included RBCs in 5% glucose (suspension medium) with identical treatment but no AgNP exposure. RBCs were counted prior to and after incubation (post third wash) with AgNPs using a hemocytometer. Capillaries were filled with RBC samples, sealed with Hematoseal, and centrifuged at 10,000 rpm for 5 min. Hematocrit values were then estimated by height from the percentage of RBCs in liquid.

2.5. Transmission Electron Microscopy (TEM) of AgNPs

Sample preparation: Filtered AgNPs (5–10 μL) were drop-casted on a carbon-coated copper grid and allowed to dry overnight. *Sample measurements:* AgNPs were imaged using a high-resolution Gatan Bioscan camera at 70 kV and were analyzed using Image J 1.46 R and Origin 8 software.

2.6. UV-Vis Absorption Spectrophotometry of AgNPs and RBCs

Sample preparation: Samples (aqueous, colloidal AgNPs, trisodium citrate solution, glucose solution, supernatants of washes, and RBCs in suspension medium before and after AgNP exposure) were placed in closed, sealed quartz cuvettes with a 1 cm path length. *Sample measurements*: UV-Vis absorption spectra were collected using a Cary 50 absorption

spectrophotometer (Agilent Inc., Santa Clara, CA, USA). The scan rate was 1200 nm min^{-1} and the spectral resolution was ~1 nm.

2.7. Raman and Surface-Enhanced Raman Spectroscopy (SERS) of AgNPs and RBCs

Sample preparation: Samples were placed directly in quartz cuvettes (filtered AgNPs) or on pre-cleaned microscope glass slides (RBCs controls in suspension medium). *Sample measurements*: Raman and SERS spectra were collected using a LabRam HR 800 system (Horiba Inc., Irvine, CA, USA) equipped with a HeNe laser (632.8 nm and 17 mW output). A high-resolution confocal Raman microscope (high-stability BX41) and Olympus objectives (100× and 50×) helped visualize and focus the laser beam on the samples. The confocal hole was set at 300 µm. The backscattering signal was recorded using a thermoelectric open-electrode CCD camera (1024 × 256 pixels), a holographic grating (600 grooves mm^{-1}), and the LabSpec v.5 software. The spectral and spatial resolutions were ~1 cm^{-1} and ~0.5–1.0 µm, respectively, at 100× magnification. The acquisition parameters were 3 cycles (automatically averaged) and 30 s of exposure (per cycle) for colloidal AgNPs. The acquisition time was reduced to 10 s to avoid photodamage of cells. RBCs were measured both individually (a single, non-aggregated RBC at a time) and in clustered form (irreversibly aggregated RBCs). The Raman and SERS spectra were processed using LabSpec v.5 and Origin 8 software. All spectra were averaged, baseline corrected and normalized with respect to the prominent band at 1550 cm^{-1}, in the spin-state marker region of hemoglobin (1500–1650 cm^{-1}). The 1500–1650 cm^{-1} broader region was processed through a spectral deconvolution. In brief, it was baseline corrected, and the peaks were individually selected using the peak finding setting in conjunction with the 2nd derivative and the quadratic Savitzky–Golay smoothing function (a 25-point window and a polynomial order of 2). Peak function iterations ($n \leq 400$) were then performed. The best fit function (Gaussian) was selected from a wide range of available functions because of its best fit convergence.

2.8. CytoViva Hyperspectral Imaging of AgNPs and RBCs

Sample preparation: Filtered AgNPs and RBCs suspended in control medium were smeared on a microscope glass slide and sealed with Vaseline. *Sample measurements:* Real-time 2-D and 3-D CytoViva images were acquired along with the corresponding hyperspectral maps (400–1000 nm) using a 3-D enhanced darkfield imaging system (CytoViva Inc., Auburn, AL, USA). The CytoViva system was equipped with an aluminum halogen source, a research-grade optical microscope, enhanced darkfield optics (special collimating lenses and mirrors), and a piezo-driven Z-axis stage. Spectra of dark current images were generated for background corrections and normalization with respect to the lamp spectrum prior to the data acquisition. High-resolution 3-D images of RBCs were created from "stacked" 2-D images, which were recorded every 100 nm in the Z direction. The spectral and spatial resolutions were about 2 nm and 128 nm (pixel size), respectively, at 100× magnification. The 3-D images and hyperspectral data were processed using the CytoViva 3-D Image Analysis ImageJ and ENVI software.

2.9. Inductively Coupled Plasma–Optical Emission Spectroscopy (ICP-OES) and Graphite Furnace Atomic Absorption Spectroscopy (GFAAS) of AgNPs and of RBCs

Sample preparation: RBC samples were chemically digested in 5 mL of nitric acid for ~15 min at room temperature. This cold digestion was followed by a hot digestion at ~180 °C with nitric acid and bleaching with 2 mL of hydrogen peroxide in glass beakers until the volume was reduced to ~200 µL. The beakers were rinsed five times with water and the contents were collected for metal analysis and mass balance calculations. The digested samples were quantitatively transferred and diluted with water to a final 2% nitric acid matrix for trace metal analysis. The AgNP samples were prepared in a similar manner, but without the hydrogen peroxide treatment. *Standard preparation*: A set of n = 11 external calibration standards, including a blank (no Ag), in 2% nitric acid were

prepared through serial dilutions from the Ag^+ stock standard solution (1000 ± 5 mg L^{-1}). The standards were in the 0–10 ng mL^{-1} of Ag range for RBC samples and 0–500 ng mL^{-1} range for colloidal AgNPs. A set of n = 6 standard additions were performed on the digested samples at the AgNP exposure level. Briefly, known concentrations of an Ag^+ standard stock solution (800 ng mL^{-1}) were added to equal volumes of sample (0.500 mL) in gradual volume increments of 0.100 mL, in the 0–0.5 mL range. *Sample measurements*: RBC samples were aspirated into the GFAAS system (GTA 120, Varian 240-FS, part of Agilent Technologies, Santa Clara, CA, USA) using an auto-sampler and the Ag content was determined at a wavelength of 328.068 nm. The acquisition parameters were: a slit width of 0.5 nm, an operating current of 40 mA, a flow rate of 0.3 L min^{-1} (argon purge gas), a drying temperature of 120 °C, a drying time of 10 s, a charring temperature of 400 °C, a charring time of 8 s, an atomization temperature of 2000 °C, and an atomization time of 5 s. AgNP samples were supplied to the ICP-OES system (Varian 71—ES) with an autosampler, at a peristaltic pump rate of 2 mL min^{-1}, nebulized, and pumped into the axially positioned quartz torch. ICP-OES measurements were carried out at the two main emission lines of Ag: 328.068 nm and 338.289 nm. The ICP-OES operating conditions were 200 kPa for the nebulizer pressure, 1.20 kW for the radio-frequency power, 15.0 L min^{-1} for the plasma flow, 1.50 L min^{-1} for the auxiliary flow, 40 s for the sample uptake delay, 45 s for the internal stabilization delay, 15 s for the rinse time, and 15 s for the read time of each replicate. A calibration check was performed every three samples.

2.10. Statistics

Each experiment was carried out in triplicate. A statistical analysis of the data was performed using the Sigma Plot 12.0 package to establish significance levels ($p < 0.05$) in spectral comparisons of bands. Student's t-test was performed on absorption maxima to establish the number of post-washes needed to remove lysed RBCs and other debris with 95% confidence intervals.

3. Results

3.1. Characterization of AgNPs

Independent batches of citrate-capped AgNPs (>1 L each) were successfully synthesized, filtered, and characterized. Figure 1 displays the results of the physicochemical characterization of filtered AgNPs. The TEM image (Figure 1A) shows the presence of small AgNPs (~10–15 nm average diameter) in the filtered colloid. The UV-Vis absorption spectra of AgNPs (Figure 1B) exhibited a characteristic LSPR peak [20,21] at ~390 nm in both water and 5% glucose, with a narrower full-width-at-half-maximum (FWHM) after filtration due to the reduction in the size distribution (5 nm ≤ AgNPs ≤ 40 nm). The Raman spectra of the filtered colloid (Figure 1C) presented three main vibrational modes characteristic to water [22] at 1648, 3232, and 3398 cm^{-1}. The SERS spectrum of the R6G test probe at 10^{-6} M (Figure S1) was recorded and compared to the Raman control spectrum of the aqueous R6G solution at 10^{-6} M to confirm the SERS-based sensing capabilities of the citrate-capped AgNPs. The CytoViva image (Figure 1D) exhibited filtered AgNPs of three increasing sizes (blue, green, and orange-red) in the center; they were surrounded by a bright "coffee-ring" of liquid around the edge of the sample. The smallest AgNPs were color coded in blue (10–15 nm) and were the most abundant, while the largest AgNPs were depicted in orange-red and were the least abundant. Out of the n = 1000 AgNPs counted with the particle counter function of ENVI, nearly 84% appeared blue (average hyperspectral maximum at ~464 nm, Figure S2), 13% were green (~554 nm), and 3% were color coded in orange-red (~637 nm).

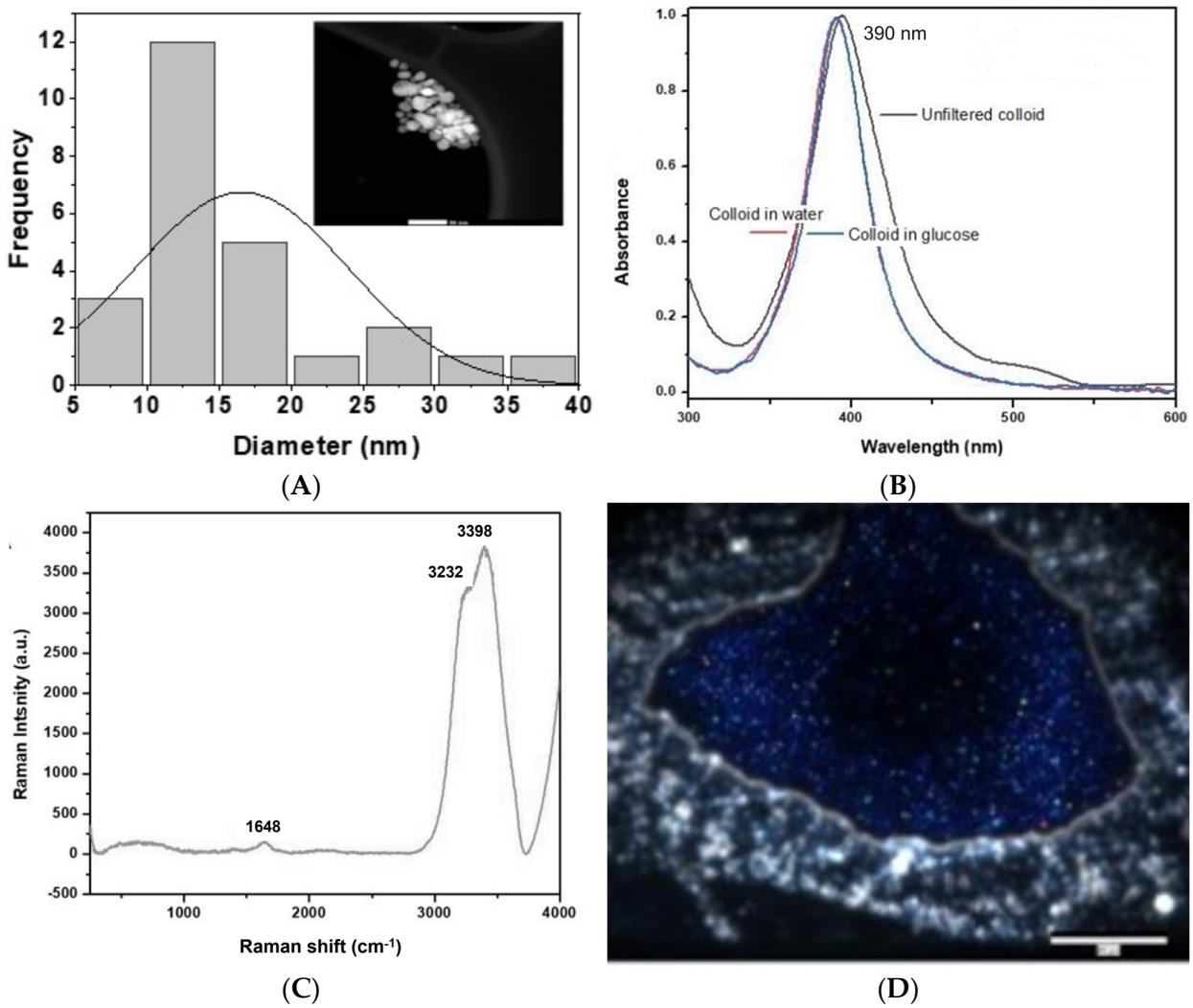

Figure 1. Physicochemical characterization of the citrate-capped colloidal silver nanoparticles (AgNPs). (**A**) TEM image showing the filtered AgNPs as round, white particles on a dark background (scale bar is 50 nm) and their (n = 25 AgNPs) relatively narrow size distribution in the 1–40 nm diameter range; (**B**) UV-Vis absorption spectra of unfiltered and filtered AgNPs in water and 5% glucose suspension medium displaying a localized surface plasmon resonance peak (LSPR) at ~390 nm; (**C**) Raman spectrum of filtered AgNPs exhibiting three main labeled peaks in the 100–4000 cm^{-1} range; and (**D**) CytoViva image of the filtered colloid in the suspension medium revealing AgNPs of different increasing sizes, color-coded in blue, green, and orange-red (scale bar is 40 μm).

3.2. RBC Absorption Spectra, Counting, and Hematocrit

UV-Vis absorption spectra of supernatants (Figure 2) were collected pre and post exposure to AgNPs to optimize the centrifugation-based wash process and to evaluate the cell lysis during the interaction with AgNPs and the suspension medium (5% glucose solution in water). In this regard, the characteristic Soret and Q absorption bands of RBC hemoglobin [10] were identified at 417, 542, and 578 nm. A paired t-test was then performed on the absorbance maxima of the most intense band, i.e., the Soret band at 417 nm, to evaluate the efficiency of RBC washes in removing lysed cells. It was implemented to test the proposed hypothesis that three washes with glucose are effective in the removal of most lysed cells and cellular debris. RBC controls in PBS had a concentration of 5.9×10^6 cells μL^{-1}. The hematocrit values of the RBC controls washed with PBS, RBC

controls washed with 5% glucose solution, and RBCs-AgNPs samples were determined to be ~32 ± 3%, ~12 ± 1%, and ~12 ± 1%, respectively.

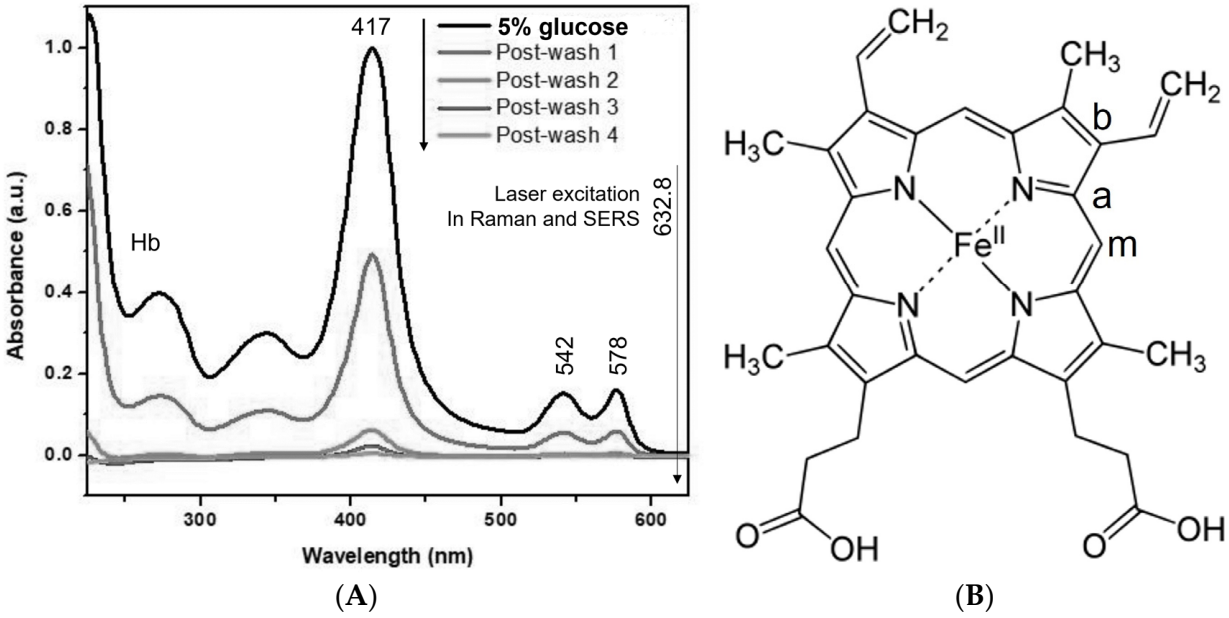

Figure 2. (**A**) Average (n = 10) absorption spectra of the RBC-AgNP samples in 5% glucose suspension medium and the supernatants collected from post-washes through four consecutive centrifugations (from top to bottom). The non-resonant Hb excitation line at 632.8 nm is provided for reference. (**B**) Schematic showing the heme group with the central iron ion coordinated to four nitrogen atoms in the center of the plane and the carbon atoms marked (a, b, and m) that are involved in marker vibrational modes. The a and b labels mark the subsequent carbon atoms of the pyrrole molecules that are adjacent to the methine (m) bridge in Hb.

3.3. Raman and Surface-Enhanced Raman Spectroscopy (SERS) of AgNPs and RBCs

The Raman spectra of RBC controls and SERS spectra of RBC-AgNP samples in suspension medium (Figure 3D) were collected after their localization with the confocal Raman microscope (Figure 3A–C). The observed vibrational modes were assigned according to the RBC literature [10–19] for both individual and clustered cells, and the key marker bands were summarized in Table S1. Aggregation of RBC controls was noticed after 24 h of incubation, but the cells were easily separated through gentle agitation. In contrast, the RBC-AgNP samples were clustered after 24 h of incubation in the suspension medium and could not be redispersed (irreversible aggregation of these RBCs), even after being vigorously vortexed (Figure 3D). The Raman spectra of the aqueous solutions of 1% citrate and 5% glucose solutions (Figure S3) were used as a reference to clarify potential spectral overlaps with the RBC peaks of interest and the tentative spectral assignment (Table S1).

A second-derivative analysis of the 1500–1650 cm^{-1} marker region revealed the presence of six peaks for the RBC controls (Figure 4A), which are indicative of a R-state characteristic to oxyHb [10–19]. These marker modes exhibited significant spectral changes upon the interaction of individual RBCs (one single cell) with AgNPs (Figure 4B). For example, the $\nu(C_a = C_b)$ stretching of pyrrole rings at 1620 cm^{-1} became negligible in relative intensity (no significant contributions to the overall fit), while the $\nu_{asym}(C_\alpha C_m)$ stretching involving the methine bridges at 1640 cm^{-1} exhibited a ~52 ± 10% decrease in the integrated area.

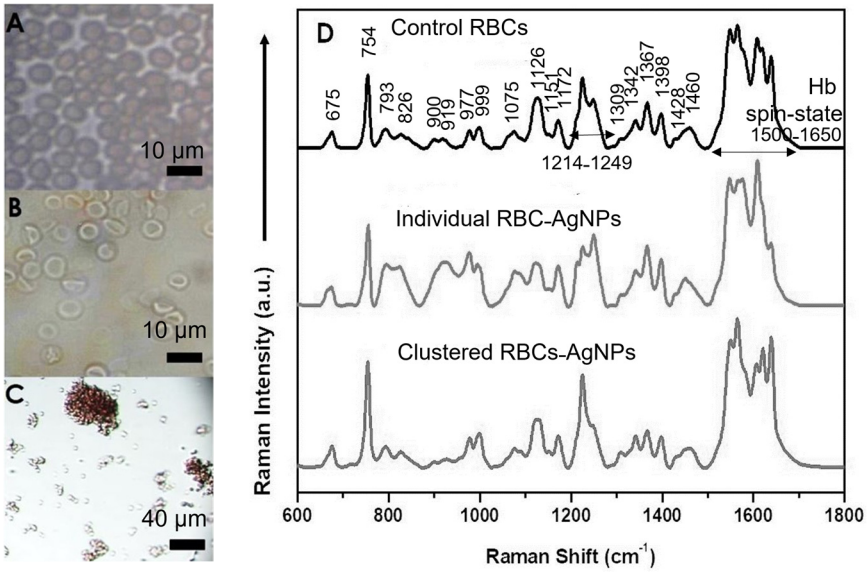

Figure 3. Confocal Raman optical images (**A**–**C**) and average (n = 10) normalized Raman spectra (**D**) of (**A**) control human red blood cells (RBCs, no AgNPs); (**B**) individual RBCs exposed to AgNPs for 1 h, and (**C**) irreversibly clustered RBCs exposed to AgNPs for 12–24 h.

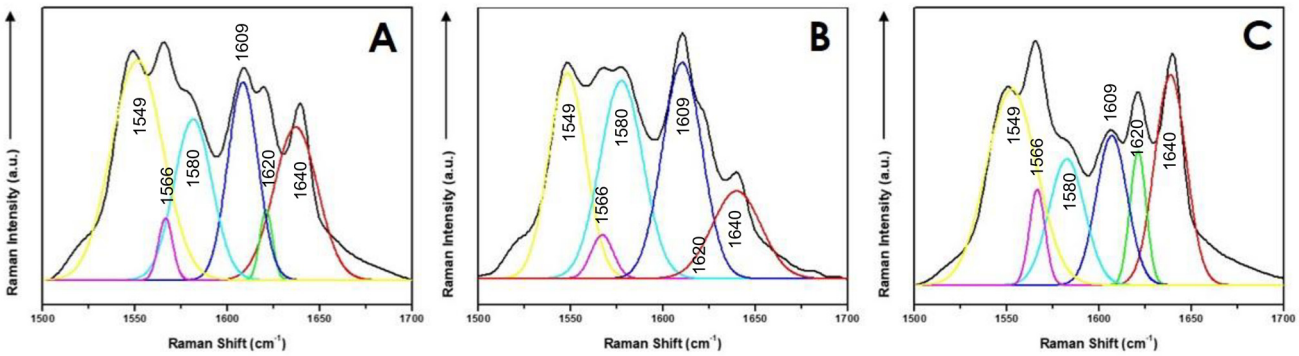

Figure 4. Deconvoluted Raman marker bands of hemoglobin in the spin-state 1500–1650 cm^{-1} spectral region: (**A**) control human red blood cells (RBCs, no AgNPs); (**B**) individual RBCs exposed to AgNPs; and (**C**) irreversibly clustered RBCs exposed to AgNPs.

3.4. CytoViva Hyperspectral Imaging of AgNPs and RBCs

Illustrative CytoViva images of control RBCs and RBCs exposed to AgNPs are given in Figures 5A and 5C, respectively. The inset in Figure 5C shows an individual RBC interacting with AgNPs of smaller sizes (color coded in blue and green) at both the extracellular and the intracellular levels. About 60% of the examined RBCs (n = ~30 cells for each condition) exhibited interactions with blue, green, or orange-red AgNPs at the extracellular membrane level. Furthermore, only 5% of the examined RBCs internalized blue or green AgNPs within the cytoplasm; no orange-red AgNPs (>25 nm) were detected intracellularly for these exposure conditions. The corresponding hyperspectral signatures of the control RBCs (Figure 5B—514, 561, and 590 nm) and the smaller, most abundant "blue" AgNPs (Figure 5D—464 nm) were provided for spectral comparisons before and after interaction with RBCs. These AgNPs were observed both extracellularly, at the membrane level of RBCs (490 nm), and intracellularly, within the cytoplasmic matrix (479 nm). The changes in position and the full-width-at-half-maximum (FWHM) of these marker peaks (Figure 5D) were quantified and summarized in Table 1 for the evaluation of the RBC-AgNP interactions. The CytoViva hyperspectral data associated with the AgNPs color-coded in "green" and "orange-red" before and after their less frequent RBC internalization are provided in Figure S2.

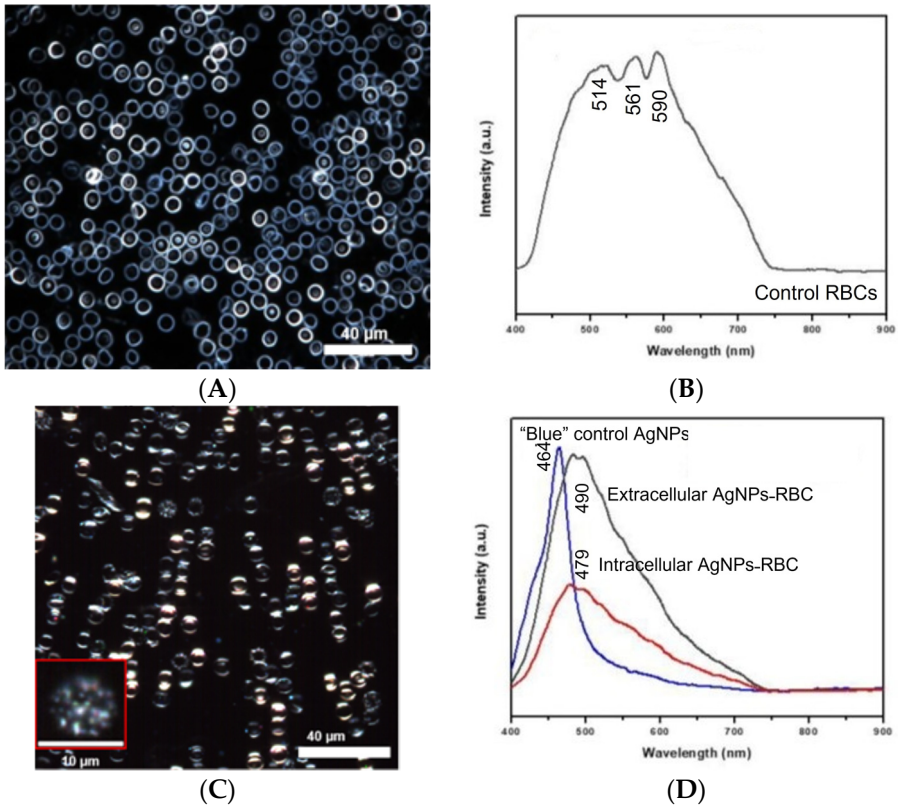

Figure 5. CytoViva image of (**A**) control human red blood cells (RBCs in suspension medium, no silver nanoparticles (AgNPs) and (**C**) RBCs exposed to AgNPs. The inset in (**C**) shows an individual RBC interacting with "blue" and "green" color coded AgNPs. Average CytoViva hyperspectra (n = 10) of (**B**) control RBCs and (**D**) filtered, "blue" AgNPs in suspension medium before and after interaction with RBCs at the membrane level (extracellular) or within the cytoplasm (intracellular).

Table 1. CytoViva hyperspectral changes (band position and full-width-at-half-maximum (FWHM)) observed in the average signatures (n = 30 cells total) of the small, most abundant "blue" AgNPs due to their interactions with RBCs (i.e., AgNPs-RBC).

"Blue" AgNPs	Band Position (nm)	FWHM (nm)
Control	464	60.6 ± 0.5
Intracellular	479	153 ± 2
Extracellular	490	142 ± 1

3.5. ICP-OES and GFAAS of AgNPs and RBCs

External calibration curves for Ag were successfully constructed using 10–11 standards, including one blank, in the 0–10 ng mL^{-1} of Ag range for both ICP-OES and GFAAS. The R^2 value was >0.9996 for the line of best fit. The limit of quantification (LOQ) was established at ~0.5 ng mL^{-1}. The amounts of Ag present in the original colloid, incubation solutions, post-washes, and RBCs were determined through interpolation from the calibration curves (Table 2). The incubation supernatant denotes the original separation of lysed RBCs exposed to AgNPs via centrifugation prior to the addition of fresh glucose solution in the first pre-wash. A calibration check was performed every three samples. The relative percent difference (RPD) in the Ag concentrations with respect to each calibration curve was <10%.

Table 2. Total amount of Ag and mass percentages of the total administered AgNPs as determined by interpolation from the GFAAS calibration curve for the samples of interest. Average values for $n = 3$ independent trials together with mean absolute deviations are provided.

Sample	Amount of Ag (μg mL^{-1})	Mass Percentage of AgNPs
Incubation mixture	34.00 ± 0.74	100%
Incubation supernatant	16.34 ± 2.30	~48.1%
Post-wash supernatants #1–3	0.825 ± 0.768	~2.4%
RBCs-AgNPs	16.24 ± 1.39	~47.8%

4. Discussion

4.1. Raman and Surface-Enhanced Raman Spectroscopy (SERS) of AgNPs and RBCs

The spontaneous Raman spectra of RBCs in suspension medium exhibited the vibrational modes characteristic to RBCs [10–19]. Most Raman bands in the control RBCs were attributed to hemoglobin (Hb) at 1640, 1620, 1609, 1580, 1566,1549, 1460, 1428, 1398, 1367, 1342, 1309, 1249-1214, 1172, 1151, 1126, 1075, 999, 977, 826, 793, 754, and 675 cm^{-1} (Table S1). Hb is the iron-containing metalloprotein that is responsible for the transport of oxygen molecules and other gases (e.g., carbon dioxide, nitric oxide, and hydrogen sulfide) from RBCs to other cells [24–26]. This chromoprotein makes up ~96% of the RBC content by dry weight and exists as hemoglobin A in humans (~64,000 Daltons) [24–26]. It is typically (up to 98%) represented by four structurally similar, globular proteins (two α and two β subunits—$\alpha_2\beta_2$) stabilized by ion interactions and hydrogen bonds. Each subunit is made of ~150 amino acid residues and is covalently bound to a non-protein heme group carrying the iron ion (ferrous Fe^{2+} or ferric Fe^{3+}) in a heterocyclic ring [24–26]. This porphyrin ring (Figure 2B) is built by four pyrrole molecules, which are cyclically connected by methine (m) bridges and have the iron ion linked in the center (Figure 2B) [24–26]. The iron ion has six coordination sites, which are occupied by four N elements of the porphyrin ring, one proximal histidine, and one free for O_2 binding [24–26]. The heme and the globular protein are tightly connected to each other by the covalent bonds of the N atoms to the imidazole ring of the proximal histidine below the porphyrin ring [24–26]. The Fe^{2+} ions of Hb can be saturated with up to four O_2 molecules through their oxidation to Fe^{3+} ions (oxyhemoglobin—oxyHb) or reversibly desaturated with O_2 (deoxyhemoglobin—deoxyHb) [24–26]. The hemoglobin form that has high O_2 affinity is called the relaxed state (R), while the form with low O_2 affinity is denoted as the taut or tense state (T) [24–26]. The ligation of one O_2 molecule pulls the Fe^{2+} ion into the plane of the porphyrin ring, which facilitates the cooperative binding of other O_2 molecules to the three remaining heme units of Hb [24–26]. This shift in conformation drags the proximal histidine and forces the plane of the ring sideways to ease the subsequent O_2 binding. Thus, the tetramer's symmetry changes upon the reversible transition from the T-state (deoxyHb) to the R-state (oxyHb) [24–26].

The Hb type was identified in prior Raman studies through the 1500–1650 cm^{-1} marker region, which is mostly due to C-C and C=C stretching modes of the porphyrin ring (Figure 3D, Tables S1 and S2) [10–19]. The spectral changes (e.g., significant changes in intensity for the $\nu(C_a = C_b)$ and $\nu_{asym}(C_\alpha C_m)$ stretching modes of the pyrrole rings and methine bridges, respectively) that were observed in this marker region after deconvolution (Figure 4) suggest the formation of deoxyHb upon the interactions with AgNPs, where the heme structure is firmly constrained in the T-state and the symmetry is higher. No significant spectral changes were observed upon the RBCs' exposure to AgNPs for Raman vibrational modes that were reported as dependent on the excitation wavelength [10]. For instance, the symmetric stretching of the pyrrole half ring at 1367 cm^{-1} was reported to become indistinguishable between the oxyHb and deoxyHb forms at longer, non-resonant excitation wavelengths such as 632.8 nm [10]. Further evidence of deoxyHb was brought by the bands corresponding to the in-plane deformations of methine ($\delta(C_mH)$) at 1250–1214 cm^{-1}) [10,16], the out-of-plane deformation of methine ($\Upsilon(C_mH)$) at

826 cm^{-1}) [10,16], and the pyrrole ring breathing (at 793 cm^{-1}) [10,16], which had different cumulative integrated areas and intensities because of the interaction of RBCs with AgNPs (Figure 3D). The methine deformation region at 1250–1214 cm^{-1} was reported to be particularly sensitive to the changes in oxygen concentration within RBCs [16]. Furthermore, the fingerprint peak at 793 cm^{-1}, which is due to the pyrrole ring breathing mode alone (no protein or lipid contributions), had a signal enhancement of 87 ± 18% (Figure 3D). As there was no observable optical electronic transition around the excitation line at 632.8 nm (Figure 2), it is believed that the observed enhancements in the individual RBC-AgNPs spectra are related to the SERS effect associated with the adsorption, i.e., favorable orientation or location of these chemical moieties at the metallic nanosurface. The AgNPs of this study are negatively charged due to the citrate layer of capping agents and thus, might be electrostatically drawn to the iron cations of the porphyrin ring or to other positively charged moieties of Hb. As a result, interactions between individual RBCs and AgNPs might occur, changing the conformation from oxyHb to deoxyHb. R-T changes in the Hb conformation of RBCs were also reported by others for large AgNPs (i.e., larger than the membrane pore sizes) [17]. For example, RBCs exposed to AgNPs of > 100 nm in diameter caused an irreversible modification in the heme conformation from the R-state (oxyHb) to the T-state (deoxyHb) due to their indirect damage of Hb. In brief, AgNPs were reported to interact with the cell surface, which subsequently altered the intracellular pH and caused blockage of cell membrane transport.

The Raman spectra of RBC controls and the SERS spectra of individual RBCs interacting with AgNPs were dominated by the vibrational modes of Hb (Figure 3D and Table S1). This is in good agreement with the literature [10–19] for both non-resonant and resonant excitations and is probably due to the highly polarizable nature of the heme prosthetic groups and their cellular abundance. However, other biomarkers of RBCs such as membrane proteins and lipids were detectable under non-resonant Hb conditions (e.g., 632.8 nm) and could serve as potential indicators of membrane alterations. The spectral quantification of these biochemical components of RBCs (proteins and lipids) can be challenging due to the overlap with dominant Hb bands, particularly under strong resonance conditions (e.g., 413 nm for the Soret electronic transition at 417 nm). The resonant contributions of the Hb groups decrease (Figure 2), while the non-resonant ones of the membrane proteins increase, upon shifting the excitation wavelength from the near-ultraviolet (413 nm) toward the near-infrared range (1064 nm). Examples of such overlapping contributions (Hb, proteins, and/or lipids) include the bands detected at 1640, 1428, 1342, 1309, 1249, 1225-1214, 1126, 1075, 999, 826, 754, and 675 cm^{-1} (Table S1) under the 632.8 nm excitation for the RBC controls. A few standalone contributions were observed at 919 and 900 cm^{-1} for generic membrane ν(C-C) protein vibrations in the Raman spectra of RBC controls, under the umbrella of a broader peak (Figure 3D). In the SERS spectra of individual RBC-AgNPs, these peaks experienced large increases (>50%) in relative intensity, perhaps due probably due to their physical proximity to the AgNPs' surface and possible chemical interactions. However, additional CytoViva measurements were carried out to help confirm the localization of AgNPs at the RBC membrane level, their cellular internalization, and interactions with key RBC biocomponents such as Hb.

Although small AgNPs (~10–15 nm on average diameter) were selected for experimental use to facilitate cellular uptake, detailed SERS spectra could be collected after 1 h of incubation of individual RBCs with AgNPs (Figure 3D). The role of AgNPs' size on the SERS enhancement has been the subject of numerous studies. We and others have shown that spherical AuNPs and AgNPs in the 30–100 nm diameter range, with an optimum size of ~50 nm in diameter, provide the maximum SERS enhancement factors [27–29]. Regardless of the exact size for optimal enhancement in a specific biological model, minuscule AgNPs will be less effective in scattering, while sizeable AgNPs approaching the scale of the excitation wavelength will become excited mostly in nonradiative modes. In both cases, diminished SERS enhancements were reported, as observed in this study. The overall SERS intensities that were observed after 1 h of incubation of individual RBCs with AgNPs were

modest (only ~10% of the spectra) when compared to the Raman spectra of RBC controls. Nevertheless, they continued to increase with increasing incubation time; ~50% of the examined RBCs had ~5 times higher signals after 24 h of storage in 5% glucose solution, at 4 °C, when compared to 1 h of exposure. This might be due to the formation of SERS "hot spots" during the irreversible clustering of RBCs. However, the overall average increase in the SERS signal (~5 times when compared to controls) associated with the clumping of RBCs came at the expense of losing most of the fine spectral changes detected during the interaction of single RBCs with AgNPs (Figures 3D and 5C). Examples include the SERS bands corresponding to individual protein vibrations at 927 and 899 cm^{-1}, the pyrrole ring breathing at 794 cm^{-1}, and the Hb marker region at 1500–1650 cm^{-1} (Table S1). The change in conformation from oxyHb to deoxyHb was difficult to observe in the irreversibly aggregated RBCs, which exhibited of 1500–1650 cm^{-1} marker region (Figure 4C) although had both spectral similarities and differences when compared to the RBC controls (Figure 4A). When RBCs are stored without anticoagulant solutions, clustering of RBCs occurs. This induced, three-dimensional (3-D) agglutination of RBCs was observed visually and through optical microscopy (Figure 3C). Aggregation of RBC controls (no AgNPs) also took place after 24 h, but the RBCs were easily separated through the gentle agitation of the solution (reversible aggregation of RBCs). However, the RBCs exposed to AgNPs for 24 h could not be redispersed even after vortexing the cells without lysing (irreversible aggregation of RBCs). The formation of inseparable clusters of RBCs-AgNPs attested to the strength of the AgNP interactions with the RBC biocomponents, which were observed by Raman and SERS. These interactions were further confirmed and clarified in several instances through subsequent CytoViva hyperspectral imaging, ICP-OES, and GFAAS measurements.

4.2. CytoViva Hyperspectral Imaging of AgNPs and RBCs

Although the Raman and SERS data offered strong evidence for the cellular uptake of AgNPs and their strong chemical interactions with Hb, little could be concluded about the size and distribution of these AgNPs within RBCs from the Raman and SERS data, particularly at the membrane level. The CytoViva 3-D function was employed to move RBCs in the Z direction toward the objective, while collecting 2-D images every 100 nm. As 2-D images (slices of the 3-D image) were gathered, AgNPs were observed at both the membrane level (extracellular) and within the cytoplasmic compartment (intracellular), and their identity was confirmed through hyperspectral signatures. The CytoViva 2-D images showed that only 5% of the imaged RBCs (n = 30) internalized AgNPs, and these AgNPs were small (<25 nm). They were identified as "blue" and "green" in color (Figure 5 and Figure S2, respectively) and experienced significant hyperspectral changes (Table 1) because of the interactions with the cellular matrices. For example, the hyperspectral band of the most abundant, "blue" AgNPs shifted from 464 nm to 479 nm and experienced a more than 2.5-fold increase in FWHM once internalized within the cytoplasm (Table 1). Furthermore, CytoViva demonstrated that over 60% of the examined RBCs had similar interactions with the citrate-capped AgNPs at the membrane level in both PBS and 5% glucose (no medium influence). These AgNPs were of all sizes (blue, green, and orange-red) and their extracellular presence was confirmed through both CytoViva images (Figure 5C) and hyperspectral signatures (Figure 5D). For example, the hyperspectral signature of the smallest "blue" AgNPs changed position from 464 nm to 490 nm, and significantly broadened (~2.3-fold) when interacting with the RBC membrane (Table 1). Similar localizations at the membrane level were reported in literature for fish RBCs [30] and membrane models [31] exposed to citrate-capped AgNPs, which were examined by hyperspectral darkfield microscopy. It was suggested that these cellular distributions are the result of strong interactions between negatively charged, citrate-capped AgNPs and cations- (e.g., quaternary ammonium on phosphatidylcholine) or thiol-containing groups (e.g., proteins) of the membrane [30,31]. Thus, CytoViva hyperspectral imaging assisted Raman and SERS by confirming the RBC-AgNP interactions and revealing the size distri-

bution and localization of AgNPs at both the membrane level (extracellularly) and within the cytoplasm (intracellularly).

4.3. ICP-OES and GFAAS of AgNPs and RBCs

ICP-OES facilitated the quantification of the total amount of Ag in the colloidal suspensions before and after filtration. The resulting concentrations were used in the incubation of RBCs with AgNPs. The suspension medium was considered to contain 100% of the administered AgNPs (Table 2), and the total amount of AgNPs absorbed by RBCs was estimated via GFAAS. GFAAS was selected over ICP-OES for measuring the RBC samples due to the very small volumes available and the one element (Ag) focus of known, maximum concentrations. The incubation supernatant that resulted from the centrifugation of the incubation mixture of RBCs and AgNPs (RBCs-AgNPs) contained about ~48.1% of the administered AgNPs. These AgNPs might be leaked out by lysed RBCs or be present in free, unbound form (no interaction with RBCs). Hematocrit values of RBC controls (~32 ± 3% for PBS versus ~12 ± 1% for 5% glucose) showed that the glucose solution may cause hemolysis in normal RBCs, but not in shrunken cells, before the glucose concentration in the suspension medium decreased. RBCs were found to expand to a normal size when the vehicle solution became hypotonic. AgNPs were not observed to cause significant hemolysis (hematocrit of ~12 ± 1% for RBCs-AgNPs). Three post-washes with glucose were found to suffice in the removal of additional unbound AgNPs (~2.4%) and lysed RBCs, after the first separation of the incubation mixture of RBC-AgNPs. This was established through the *t*-test (Table S3). An insignificant percentage (≤0.15%) of unbound AgNPs were removed during the third and final wash of the RBC-AgNP samples post incubation. The final suspension of RBCs was found to have absorbed ~47.8% of the originally administered AgNPs. This is a relatively high percentage, when taking into consideration the negative charge of both the citrate-capped AgNPs and the cell membrane. High cellular absorptions (50–65%) have also been reported by others in human cells such as 16HBE14o pulmonary epithelial cells exposed to citrate-capped AgNPs (BioPure from NanoCompsix Inc., San Diego, CA, USA) [32]. This uptake was found to be dependent on the AgNP size and the composition of the medium (highest internalization percentage of 65% for AgNPs of 50 nm and no fetal calf serum), but no conclusions were drawn with respect to the cellular uptake mechanism [32].

Herein, it was hypothesized and then experimentally established through CytoViva hyperspectral signatures that only small AgNPs ("blue" and "green") were internalized by RBCs probably through passive and/or facilitated diffusions of AgNPs across the cellular membrane (Figure S5) [30]. This was in part due to the small size of the membrane ion channels and lack of receptor mediated endocytosis in normal, mature RBCs. Numerous studies have reported the cellular uptake of small nanoparticles (<10 nm) through a non-endocytic passive penetration process. For example, the zwitterionic D-penicillamine-coated quantum dots (DPA-QDs, 4 nm) were found to electrostatically interact with the lipid bilayer membrane, and thereby, to render it more flexible [33]. This softening facilitated the passive penetration of the DPA-QDs without affecting the overall membrane integrity or causing any pore formation [33]. Thus, it is possible that the small "blue" and "green" AgNPs of this study (<10 nm) might also enter cells through passive or facilitated diffusion. In addition, shriveled cellular shapes and physical membrane damage could further enable the internalization of larger AgNPs (<25 nm); these changes in cell structure were observed in some of the CytoViva images of RBCs exposed to AgNPs. No conclusions could be drawn about the observed decreases in hematocrit values, because similar hemolysis occurred in both RBC controls washed with 5% glucose solution and RBC-AgNP samples suspended in 5% glucose. This is not uncommon, as ultrafine polystyrene particles (<0.1 μm) and AuNPs (25 nm in diameter) were found to cross the human RBC membrane but were not membrane bound [34]. The proposed passive uptake included "adhesive interactions" such as electrostatic, Van der Waals, or steric interactions, where thermal capillary waves and line tension play a significant role in the NP cellular uptake [34]. Furthermore, a

wide variety of cationic NPs made of both organic (peptides and polycationic polymers) and inorganic (Au-NH_2, SiO_2-NH_2) materials have been shown to penetrate membrane-mimicking supported lipid bilayers (SLB) through the disruption of lipid bilayers and nanoscale hole formation [35]. Overall, GFAAS supported the proposed hypotheses for the AgNP uptake mechanisms and the observed Raman and CytoViva interactions through the quantification of the total amount of AgNPs absorbed by RBCs.

5. Conclusions

Overall, this study showed that Raman spectroscopy and SERS can be instrumental in future biomedical and forensic applications due to their capabilities of molecularly fingerprinting blood components such as RBCs and their interactions with metallic nanomaterials such as AgNPs designed for drug delivery or imaging. Herein, Raman and SERS offered strong spectral evidence for the uptake and chemical interactions of citrate-capped AgNPs with human RBCs (particularly Hb) and the subsequent change in conformation from oxyHb to deoxyHb. As the Raman and SERS measurements were carried out under non-resonant excitation conditions at 632.8 nm, both Hb and membrane contributions could be identified in the collected Raman and SERS spectra. However, only a few generic AgNP-protein vibrational modes had well-separated peaks and provided clear evidence of the interactions between AgNPs and the RBC membrane. This was probably due to its high abundance (Hb makes up most of RBCs' dry weight) and the dominant Raman bands of Hb, which overlapped with most of the cell membrane peaks. These contributions could be separated in future studies using excitation conditions that are pre-resonant or resonant with the electronic transitions of membrane lipids and proteins in the near-infrared range (1064 nm). Nevertheless, this will come at the expense of the Hb characteristic Raman modes, whose relative intensity will be diminished. This study showed that CytoViva hyperspectral imaging and GFAAS could be utilized as complementary tools to overcome these Raman/SERS challenges associated with the use of a single excitation line (in the biocompatible red or near-infrared range) and the limited resolutions of a confocal Raman microscope (limited by the diffraction of white light). In brief, GFAAS and CytoViva indicated that the cellular absorption of small AgNPs (<10 nm) was significant, mostly at membrane level (60% of the examined RBCs), and size dependent. No large AgNPs (>25 nm) were internalized or formed through aggregation inside the RBCs, even after prolonged exposure times (12–24 h). CytoViva confirmed the RBC-AgNP interactions through hyperspectral signatures and facilitated the label-free localization of AgNPs at both the cell membrane (extracellularly) and within the cytoplasmic compartment (intracellularly). In contrast to the best but rather modest resolution of confocal Raman microscopes (~0.2 μm laterally and ~0.6 μm axially—seldomly achieved) [36,37], the CytoViva hyperspectral microscope could observe AgNPs as small as 10–20 nm in diameter directly into live cells (images of 700,000 pixels at 100× magnification). This was rapidly achieved with the help of enhanced darkfield optics and at a level not possible with traditional confocal Raman microscopes [38]. GFAAS verified the AgNP uptake by quantifying the total amount of Ag present intracellularly and extracellularly, i.e., interacting with RBCs (~48% of the administered dose of AgNPs by mass). GFAAS has been deemed the gold standard for accurately quantifying the total uptake of metallic nanoparticles by cells, which traditional Raman or SERS approaches cannot achieve [39,40]. Irreversible clumping of RBCs was noted because of the exposure to AgNPs for 24 h, at 4 °C, in 5% glucose. This raises concerns with respect to the toxicity of citrate-capped AgNPs, which are generally considered biocompatible due to their coating [41,42]. For example, citrate-coated AgNPs (6 nm in average diameter) had minimum bactericidal concentrations for Gram-positive (*Staphylococcus aureus*) and Gram-negative (*Pseudomonas aeruginosa*) bacteria that were smaller than the AgNP concentrations leading to cytotoxic effects in UMR-106 osteoblastic cells [41]. Thus, the use of citrate-capped AgNPs for health-related applications should be carefully assessed as irreversible RBC agglutination might occur within the cardiovascular system due to the strong RBC-AgNP interactions.

Supplementary Materials: The following supporting information can be downloaded at: https://www.mdpi.com/article/10.3390/chemosensors11070353/s1, Figures S1–S5 and Tables S1–S3 presenting additional Raman, SERS, CytoViva hyperspectral imaging and GFAAS data.

Author Contributions: Conceptualization, K.L.W., P.K.A. and I.E.P.; methodology: K.L.W., P.K.A., N.C.A. and I.E.P.; software: K.L.W., P.K.A. and I.E.P.; validation: K.L.W., P.K.A., N.C.A. and I.E.P.; formal analysis, K.L.W., P.K.A., K.G.K., I.T.M., N.C.A. and I.E.P.; investigation, K.L.W., P.K.A. and I.E.P.; data curation: K.G.K., I.T.M. and I.E.P.; writing—original draft preparation, K.L.W. and I.E.P.; writing—review and editing, K.L.W., P.K.A., N.C.A., K.G.K., I.T.M., N.C.A. and I.E.P.; supervision, N.C.A. and I.E.P.; project administration, N.C.A. and I.E.P.; funding acquisition, N.C.A. and I.E.P. All authors have read and agreed to the published version of the manuscript.

Funding: The USA National Science Foundation Awards #1438340 and #1726095 are highly acknowledged. Texas A&M University Corpus Christi (TAMU-CC), TX, USA, and Wright State University (WSU), OH, USA, are highly acknowledged for their support. The 2022 TAMU-CC Student Research Competition Award granted to Kyra Kaiser is highly acknowledged.

Institutional Review Board Statement: Ethical review and approval were waived for this study due to not meeting the definition of human subject research (IRB #06874 9 March 2020, and #6034, 10 December 2015, WSU, USA).

Informed Consent Statement: Not applicable.

Data Availability Statement: Wells, K.L. Analytical-based methodologies for monitoring the uptake, distribution, and molecular interaction of silver nanoparticles with human red blood cells. Master's Thesis, WSU, Dayton, OH, USA, 2018.

Acknowledgments: John Ryan and Kanel Sushil at the Wright Patterson Air Force Base, OH, USA, are highly acknowledged for their assistance with the TEM data acquisition. The authors would like to thank Garrett VanNess and Joseph Solch for the assistance with Wright State University instrumentation.

Conflicts of Interest: The authors declare no conflict of interest.

References

1. Qiu, Y.; Kuang, C.; Liu, X.; Tang, L. Single-molecule surface-enhanced Raman spectroscopy. *Sensors* **2022**, *22*, 4889. [CrossRef] [PubMed]
2. Moskovits, M. Surface-enhanced Raman spectroscopy: A brief retrospective. *J. Raman Spectrosc.* **2005**, *36*, 485–496. [CrossRef]
3. Kneipp, K. Surface-enhanced Raman scattering. *Phys. Today* **2007**, *60*, 40–46. [CrossRef]
4. Blackie, E.J.; Le Ru, E.C.; Etchegoin, P.G. Single-molecule surface-enhanced Raman spectroscopy of nonresonant molecules. *J. Am. Chem. Soc.* **2009**, *131*, 14466–14472. [CrossRef]
5. Xu, H.; Aizpurua, J.; Käll, M.; Apell, P. Electromagnetic contributions to single-molecule sensitivity in surface-enhanced Raman spectroscopy. *Phys. Rev. E* **2000**, *62*, 4318–4324. [CrossRef]
6. Braun, G.; Pavel, I.; Morrill, A.R.; Seferos, D.S.; Bazan, G.C.; Reich, N.O.; Moskovits, M. Chemically patterned microspheres for controlled nanoparticle assembly in the construction of SERS hot spots. *J. Am. Chem. Soc.* **2007**, *129*, 7760–7761. [CrossRef]
7. Kim, N.; Hwang, W.; Baek, K.; Rohman, M.R.; Kim, J.; Kim, H.W.; Mun, J.; Lee, S.Y.; Yun, G.; Murray, J.; et al. Smart SERS hot spots: Single molecules can be positioned in a plasmonic nanojunction using host-guest chemistry. *J. Am. Chem. Soc.* **2018**, *140*, 4705–4711. [CrossRef]
8. Tan, Y.; Yan, B.; Xue, L.; Li, Y.; Luo, X.; Ji, P. Surface-enhanced Raman spectroscopy of blood serum based on gold nanoparticles for the diagnosis of the oral squamous cell carcinoma. *Lipids Health Dis.* **2017**, *16*, 73. [CrossRef]
9. Boyd, S.; Massimo, B.F.; Bertino, F.; Ye, D.; White, L.S.; Seashols, S.J. Highly sensitive detection of blood by surface enhanced Raman scattering. *J. Forensic. Sci.* **2013**, *58*, 753–756. [CrossRef]
10. Wood, B.R.; Kochan, K.; Marzec, K.M. Resonance Raman spectroscopy of hemoglobin in red blood cells. In *VibrationalSpectroscopy in Protein Research*, 1st ed.; Ozaki, Y., Baranska, M., Lednev, I.K., Wood, B.R., Eds.; Elsevier Inc.: Amsterdam, The Netherlands, 2020; pp. 375–414.
11. Dybas, J.; Alcicek, F.C.; Wajda, A.; Kaczmarska, M.; Zimna, A.; Bulat, K.; Blat, A.; Stepanenko, T.; Mohaissen, T.; Szczesny-Malysiak, E.; et al. Trends in biomedical analysis of red blood cells—Raman spectroscopy against other spectroscopic, microscopic and classical techniques. *TrAC* **2022**, *146*, 116481. [CrossRef]
12. Barkur, S.; Chidangil, S. Surface-enhanced Raman spectroscopy study of red blood cells and platelets. *J. Biomol. Struct. Dyn.* **2019**, *37*, 1090–1098. [CrossRef] [PubMed]

13. Harada, I.; Takeuchi, H. Raman and ultraviolet resonance Raman spectra of proteins and related compounds. In *Spectroscopy of Biological Systems*, 1st ed.; Clark, R.J.H., Hester, R.E., Eds.; John Wiley & Sons: Chichester, UK, 1986; Volume 13, pp. 113–175.
14. Drescher, D.; Büchner, T.; McNaughton, D.; Kneipp, J. SERS reveals the specific interaction of silver and gold nanoparticles with hemoglobin and red blood cell components. *Phys. Chem. Chem. Phys.* **2013**, *15*, 5364–5373. [CrossRef] [PubMed]
15. Hu, S.; Smith, K.M.; Spiro, T.G. Assignment of protoheme resonance Raman spectrum by heme labeling in myoglobin. *J. Am. Chem. Soc.* **1996**, *118*, 12638–12646. [CrossRef]
16. Wood, B.R.; Caspers, P.; Puppels, G.J.; Pandiancherri, S.; McNaughton, D. Resonance Raman spectroscopy of red blood cells using near-infrared laser excitation. *Anal. Bioanal. Chem.* **2007**, *387*, 1691–1703. [CrossRef] [PubMed]
17. Bankapur, A.; Barkur, S.; Chidangil, S.; Mathur, D. A micro-Raman study of live, single red blood cells (RBCs) treated with $AgNO_3$ nanoparticles. *PLoS ONE* **2014**, *9*, e103493. [CrossRef]
18. Premasiri, W.R.; Lee, J.C.; Ziegler, L.D. Surface-enhanced Raman scattering of whole human blood, blood plasma, and red blood cells: Cellular processes and bioanalytical sensing. *J. Phys. Chem. B* **2012**, *116*, 9376–9386. [CrossRef]
19. Chen, F.; Flaherty, B.R.; Cohen, C.E.; Peterson, D.S.; Zhao, Y. Direct detection of malaria-infected red blood cells by surface-enhanced Raman spectroscopy. *Nanomedicine* **2016**, *12*, 1445–1451. [CrossRef]
20. Lee, P.C.; Meisel, D. Adsorption and surface-enhanced Raman of dyes on silver and gold sols. *J. Phys. Chem.* **1982**, *86*, 3391–3395. [CrossRef]
21. Wan, Y.; Guo, Z.; Jiang, X.; Fang, K.; Lu, X.; Zhang, Y.; Gu, N. Quasi-spherical silver nanoparticles: Aqueous synthesis and size control by the seed-mediated Lee-Meisel method. *J. Colloid Interface Sci.* **2013**, *394*, 263–268. [CrossRef]
22. Trefry, J.C.; Monahan, J.L.; Weaver, K.M.; Meyerhoefer, A.J.; Markopolous, M.M.; Arnold, Z.S.; Wooley, D.P.; Pavel, I.E. Size selection and concentration of silver nanoparticles by tangential flow ultrafiltration for SERS-based biosensors. *J. Am. Chem. Soc.* **2010**, *132*, 10970–10972. [CrossRef]
23. Anders, C.B.; Baker, J.D.; Stahler, A.C.; Williams, A.J.; Sisco, J.N.; Trefry, J.C.; Wooley, D.P.; Sizemore, I.E. Tangential flow ultrafiltration: A "green" method for the size selection and concentration of colloidal silver nanoparticles. *J. Vis. Exp.* **2012**, *68*, e4167. [CrossRef] [PubMed]
24. Thomas, C.; Lumb, A.B. Physiology of haemoglobin. *CEACCP* **2012**, *12*, 251–256. [CrossRef]
25. Gell, D.A. Structure and function of haemoglobines. *Blood Cells Mol. Dis.* **2018**, *70*, 13–42. [CrossRef] [PubMed]
26. Ahmed, M.H.; Ghatge, M.S.; Safo, M.K. Hemoglobin: Structure, function, and allostery. *Subcell Biochem.* **2020**, *94*, 345–382. [PubMed]
27. Israelsen, N.D.; Hanson, C.; Vargis, E. Nanoparticle properties and synthesis effects on surface-enhanced Raman scattering enhancement factor: An introduction. *Sci. World J.* **2015**, *2015*, 124582. [CrossRef]
28. Dorney, K. A Chemical-Free Approach for Increasing the Biochemical Surface-Enhanced Raman Spectroscopy (SERS)-Based Sensing Capabilities of Colloidal Silver Nanoparticles. Master's Thesis, Wright State University, Dayton, OH, USA, 2014.
29. Stamplecoskie, K.G.; Scaiano, J.C.; Tiwari, V.S.; Anis, H. Optimal size of silver nanoparticles for surface-enhanced Raman spectroscopy. *J. Phys. Chem. C* **2011**, *115*, 1403–1409. [CrossRef]
30. Chen, L.Q.; Fang, L.; Ling, J.; Ding, C.Z.; Kang, B.; Huang, C.Z. Nanotoxicity of silver nanoparticles to red blood cells: Size dependent adsorption, uptake, and hemolytic activity. *Chem. Res. Toxicol.* **2015**, *28*, 501–509. [CrossRef]
31. Bhat, A.; Huan, K.; Cooks, T.; Boukari, H.; Lu, Q. Probing interactions between AuNPs/AgNPs and giant unilamellar vesicles (GUVs) using hyperspectral dark-field microscopy. *Int. J. Mol. Sci.* **2018**, *19*, 1014. [CrossRef]
32. Kettler, K.; Krystek, P.; Giannakou, C.; Hendricks, A.J.; de Jong, W.H. Exploring the effect of silver nanoparticle size and medium composition on uptake into pulmonary epithelial 16HBE14o-cells. *J. Nanopart. Res.* **2016**, *18*, 182. [CrossRef]
33. Wang, T.; Bai, J.; Jiang, X.; Nienhaus, G.U. Cellular Uptake of Nanoparticles by Membrane Penetration: A Study Combining Confocal Microscopy with FTIR Spectroelectrochemistry. *ACS Nano* **2012**, *6*, 1251–1259. [CrossRef]
34. Geiser, M.; Rothen-Rutishauser, B.; Kapp, N.; Schuerch, S.; Kreyling, W.; Schulz, H.; Semmler, M.; Im Hof, V.; Heyder, J.; Gehr, P. Ultrafine particles cross cellular membranes by nonphagocytic mechanisms in lungs and in cultured cells. *Environ. Health Perspect.* **2005**, *113*, 1555–1560. [CrossRef] [PubMed]
35. Leroueil, P.R.; Berry, S.A.; Duthie, K.; Han, G.; Rotello, V.M.; McNerny, D.Q.; Bakerm, J.R., Jr.; Orr, B.G.; Holl, M.M. Wide varieties of cationic nanoparticles induce defects in supported lipid bilayers. *Nano Lett.* **2008**, *8*, 420–424. [CrossRef] [PubMed]
36. Giridhar, G.; Manepalli, R.R.K.N.; Apparao, G. Chapter 7—Confocal Raman Spectroscopy. In *Spectroscopic Methods for Nanomaterials Characterization*; Elsevier: Amsterdam, The Netherlands, 2017; pp. 141–161. [CrossRef]
37. Elliot, A.D. Confocal Microscopy: Principles and Modern Practices. *Curr. Protoc. Cytom.* **2020**, *92*, e68. [CrossRef]
38. CytoViva in CytoViva Hyperspectral Microscope at CytoViva | Enhanced Darkfield Hyperspectral Microscope | Products. Available online: https://www.cytoviva.com (accessed on 18 June 2023).
39. Aguilar, Z.P. *Nanomaterials for Medical Applications*; Elsevier: Amsterdam, The Netherlands, 2013; 2.1.9: Atomic Absorption Spectroscopy. [CrossRef]
40. Svitkova, B.; Selc, M.; Nemethova, V.; Razga, F.; Gabelova, A.; Ursinyova, M.; Babelova, A. Plate reader spectroscopy as an alternative to atomic absorption spectroscopy for the assessment of nanoparticles cellular uptake. *Heliyon* **2022**, *8*, e11595. [CrossRef]

41. Flores, C.Y.; Minan, A.G.; Grillo, C.A.; Salvarezza, R.C.; Vericat, C.; Schilardi, P.L. Citrate-capped silver nanoparticles showing good bacterial effect against both plankytonic and sessile bacteria and a low cytotoxicity to osteoblastic cells. *ACS Appl. Mater. Interfaces* **2013**, *5*, 3149–3159. [CrossRef]
42. Ma, C.; Gerhard, E.; Lu, D.; Yang, J. Citrate chemistry and biology for biomaterials design. *Biomaterials* **2018**, *178*, 383–400. [CrossRef] [PubMed]